IN-02-CR
97503
8P.

HYPERSONIC FLOW ANALYSIS

NASA-Ames Research Center
Cooperative Agreement No. NCC 2-440

Final Report for the Period

September 1, 1986 - August 31, 1987

Submitted by Chuen-Yen Chow, Principal Investigator

James S. Ryan, Research Assistant

Department of Aerospace Engineering Sciences

University of Colorado

Boulder, Colorado 80309-0429

(NASA-CR-181332) HYPERSONIC FLOW ANALYSIS Final Report, 1 Sep. 1986 - 31 Aug. 1987 (Colorado Univ.) 8 p Avail: NTIS HC A02/MF A01
CSCL 01A
N87-27646
G3/02
Unclas
0097503

Development of a Zonal CFD Code for Hypersonic Flows

INTRODUCTION:

As detailed models of the National Aerospace Plane become available, CFD codes will be required to accurately model flows over those models at Mach numbers up to 25. No current CFD code can handle both the high Mach number conditions and the complex geometries which will be required.

Codes do exist which can produce Navier-Stokes solutions about simplified body shapes in the hypersonic regime. Four such codes have recently been compared by Edwards, et al., using a bicone shape and a generic elliptical all-body vehicle(1). While all of these codes are fairly accurate, they will become increasingly difficult to apply as model geometries become more complex.

TNS (Transonic Navier-Stokes) is a CFD code which has been successfully applied to geometries as complex as the F-16A (2). The zonal capability of TNS allows a complex body to be modeled as an assemblage of relatively simple zones, with appropriate boundary conditions between zones. TNS was developed for transonic flow simulation over bodies which are best modeled using several zones, either due to the complexity of the geometry or to central memory limitations. The flow solver it uses is a diagonalized Beam-Warming method (3). While results in the transonic regime are very good, attempts to apply TNS to hypersonic flows have shown that this flow solver is probably a poor choice for hypersonic cases.

This situation suggests that a synthesis of the TNS geometry capability with a more appropriate flow solver might produce a code capable of modeling detailed hypersonic vehicle designs.

One flow solver selected for testing is that of F3D(4), which has been applied to STS at a Mach number of 7.9 and to a generic wing-body hypersonic configuration at Mach 25 (5). F3D was also included in the four-code comparison mentioned above.

The work described here is based on a version of F3D provided by Y. Rizk, and a version of TNS which was modified for high-sweep cases by Jeff Cordova.

TNS Testing:

The existing TNS code has been tested to determine the highest Mach number at which solutions can be obtained.

A generic elliptical all-body configuration was selected as a test case, since it represents the overall shape of a hypersonic vehicle in a simple way. A 2-D elliptic grid generator developed by Cordova was used to create Y-Z cross sectional grids about the body, and the grids were simply stacked in the X (streamwise) direction to create a three-dimensional grid. A more optimal grid could have been generated with a true three-dimensional method, but this was not done, since the flow solver will be required to tolerate some imperfections in grid orthogonality and smoothness as models become more complex.

Once the grid was obtained, tests were made at increasing Mach numbers. Table 1 lists the cases which were run. The number of iterations shown reflects the time required to select effective time step and dissipation parameters, and may be much greater than the number of steps which would be required for another run of the same case. In all cases, the Reynolds number was 0.75E+06.

For Mach numbers up to about 4, it proved fairly easy to obtain solutions. Each run was started from freestream conditions. A moderate increase in the fourth-order artificial dissipation was sufficient to maintain stability in the early steps, and the dissipation could be reduced to 0.01 or less after one order of magnitude convergence had been achieved. This value is the same as is used in transonic cases.

When the Mach number reached 6, the dissipation parameter had to be set more carefully. It was found that the stability of the code peaked sharply when the correct dissipation was used (Figure 1). Unfortunately, the correct value varied with Mach number and with the number of time steps which had been made, so the optimization must be repeated several times for each case.

At a Mach number of 7.4, there was no longer a stability peak for any positive value of the dissipation parameter (Figure 1). The solution could no longer be obtained from free stream conditions. Instead, the Mach 6 solution was used as a starting solution, and the outer boundary conditions were ramped slowly up to Mach 7.4 . Solutions for positive angles of attack were obtained by similar slow changes in the boundary conditions. At 4 degrees, a solution was obtained, but at 6 degrees an instability in the wake region prevented convergence.

Solutions were not obtained for Mach numbers greater than 7.4, even at zero angle of attack. While such solutions are not impossible, the increasing computational effort required seems prohibitive.

CNS Development:

In order to obtain solutions at higher Mach numbers, and to improve shock capturing in both supersonic and hypersonic conditions, a new code is being developed. The new code will be called CNS (Compressible Navier-Stokes). It will retain the zonal geometry capability of TNS, while incorporating a flow solver more suited to high Mach number cases.

One of the flow solvers under consideration for CNS is the partially flux-split flow solver of F3D. The solver provides upwinding along one coordinate direction. In order to test this option, the F3D solver has been included as an option in the existing high-sweep TNS code. So far, no solutions have been generated with the new code.

RESULTS:

The solutions which have been obtained with TNS on the all-body do not correspond in Mach number, Reynolds number, and angle of attack to any published results obtained by other methods. Edwards, et al.(1) provide comparisons of results from four codes which have been validated on a bicone configuration and applied to the all-body geometry. To date this is the only data available, since no experimental results have been released for publication. Extensive validation will begin only after a flow solver has been incorporated which can give solutions over a wider range of Mach numbers.

Figures 2 and 3 are included as examples of the data to be used for validation. Figure 2 shows boundary layer profiles at 3 X stations along the body centerline (symmetry plane) the conditions are M = 7.4, Re = 0.75e+06, alpha = 0 degrees. Figure 3 shows the pressure coefficient along the centerline, above and below the body. The conditions are the same as for Figure 2, except at 4 degrees angle of attack.

CONCLUSIONS:

While the zonal grid system of TNS provides excellent modeling of complex geometries, improved shock capturing, and a higher Mach number range will be required if flows about hypersonic aircraft are to be modeled accurately.

A new CFD code, CNS (Compressible Navier-Stokes), is under development to combine the required high Mach number capability with the existing TNS geometry capability. One of several candidate flow solvers for inclusion in CNS is that of F3D. This upwinding flow solver promises improved shock capturing, and more accurate hypersonic solutions solutions overall, compared to the solver currently used in TNS.

REFERENCES:

1. Edwards, T. A., Chaussee, D., Lawrence, S., and Rizk, Y., "Comparisons of Four CFD Codes as Applied to a Hypersonic All-body Vehicle," AIAA paper 87-2642, 1987.

2. Flores, J., Chaderjian, N. M., and Sorenson, R. L.; "Simulation of Transonic Viscous Flow over a Fighter-like Configuration Including Inlet," AIAA paper 87-1199.

3. Pulliam, T. H., and Chaussee, D. S.; "A Diagonal Form of an Implicit Approximate-Factorization Algorithm," Journal of Computational Physics, Vol. 39, No. 2, 1981, pp. 347-363.

4. Ying, S. X., Steger, J. L., Schiff, L. B., and Baganoff, D.; "Numerical Simulation of Unsteady, Viscous, High Angle of Attack Flows Using a Partially Flux Split Algorithm," AIAA Paper 86-2179.

5. Rizk, Y., Chaussee, D., and Steger, J.; "Numerical Simulation of the Hypersonic Flow Around Lifting Vehicles.", NASA TM 89444, April, 1987.

Table 1

Cases tested using the Pulliam-Chaussee diagonalized algorithm in TNS with the all-body configuration.

Freestream Mach Number	Alpha (degrees)	Grid Size (total)	Iterations	Convergence (orders of magnitude drop in L2 norm of the residual) inner zones	outer zones
7.4	6.0	114,324	735	0.2-2.2	0.8-3.6
7.4	4.0	114,324	1200	3.0	2.-5.
7.4	4.0	114,324	1702	4.0	3.-6.
7.4	2.0	114,324	900	1.5-2.6	0.0-3.9
7.4	0.0	114,324	3000	4.-6.	7.
7.4	0.0	114,324	115	-	-
6.0	0.0	114,324	2300	4.-6.	2.-5.
4.0	0.0	348,595	1200	5.	2.4-5.2
2.0	2.0	348,595	1550	4.5	2.3-4.4
2.0	2.0	114,324	900	3.9-4.5	2.-3.6

Stability Optimization

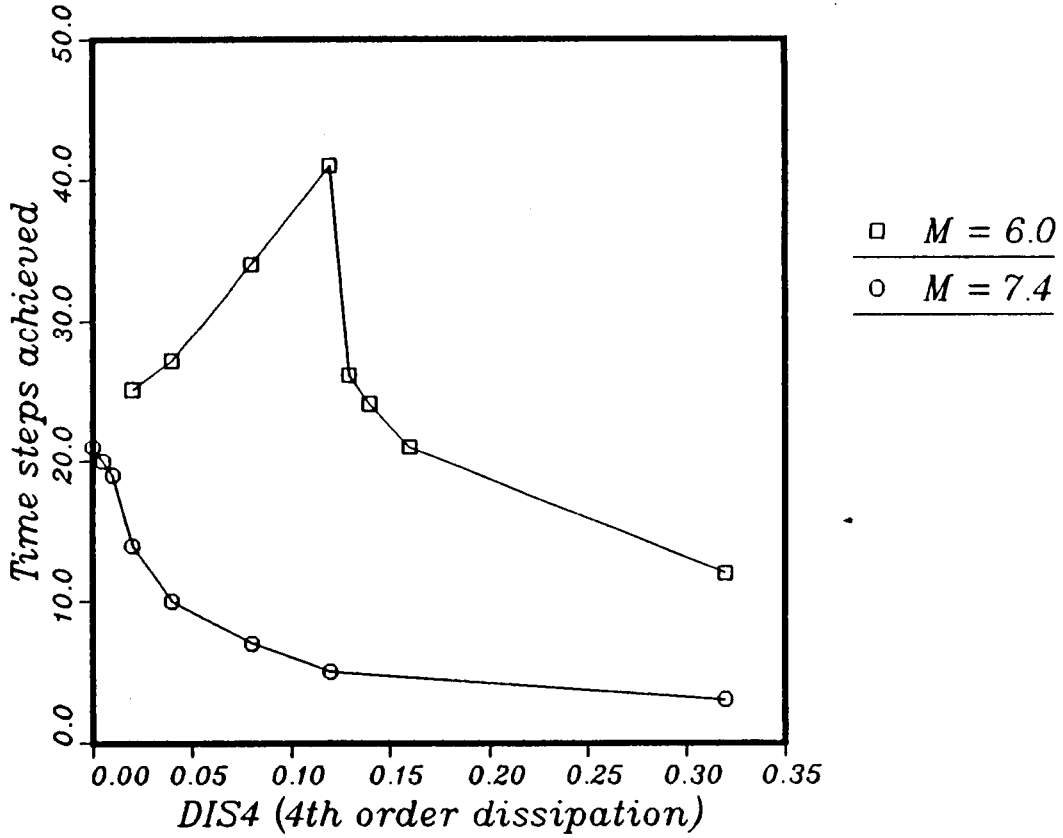

FIGURE 1

Curves for optimization of the artificial dissipation. At Mach 6, repetition of this method led to a stable solution. At Mach 7, it was not possible to start from freestream.

Boundary Layer Profiles

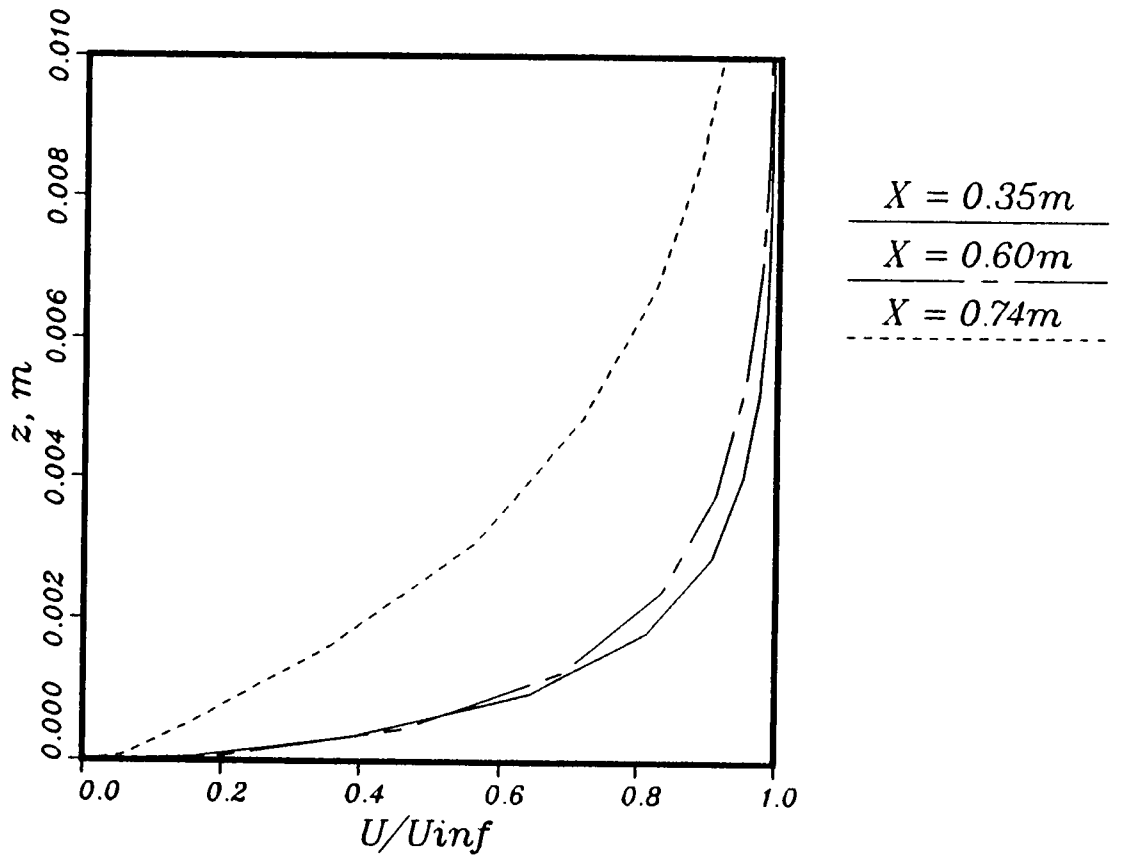

FIGURE 2

Values at 3 streamwise stations on the centerline
Mach 7.4, alpha = 0 degrees, Re = 0.75E+06

Pressure Coefficients

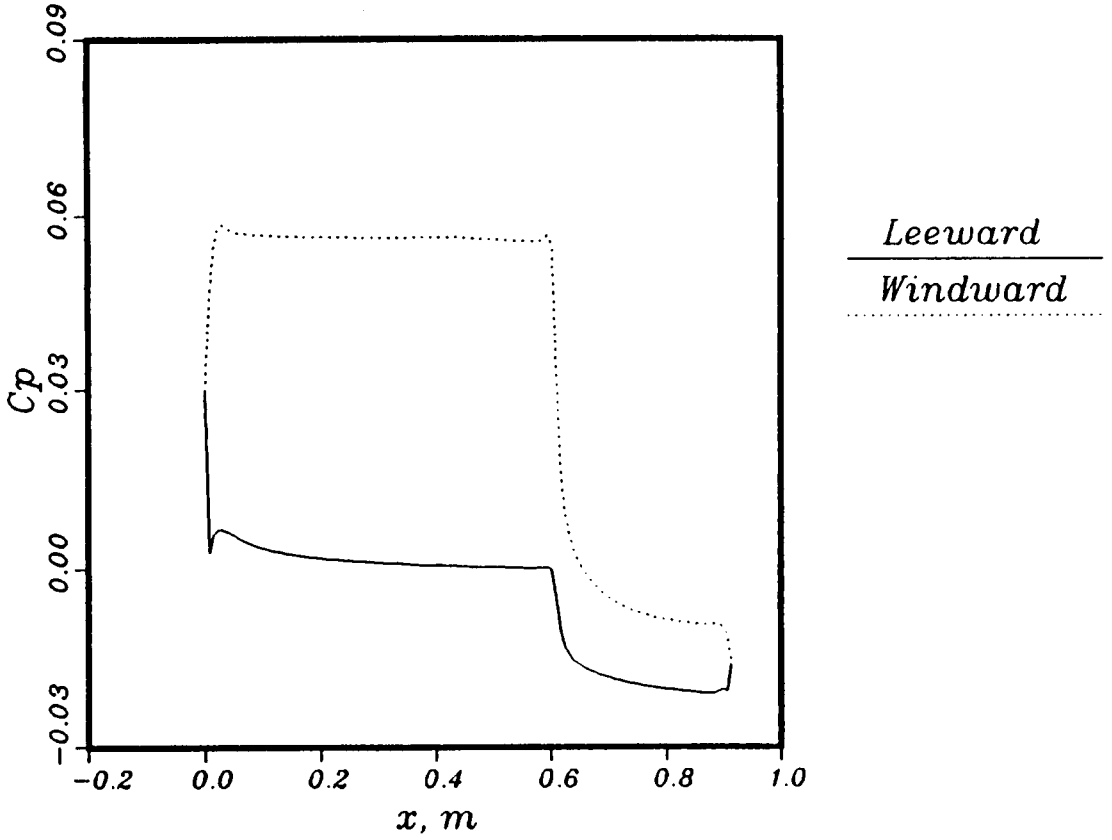

FIGURE 3

Values along the all−body centerline

Mach 7.4, alpha = 4 degrees, Re = 0.75E+06

Figure 3. Zero-Total-Pressure-Loss Euler, Set (2), Sharp-edged Wing, 64X64 Cell, M_∞=2.0, α=10^0, β=70^0, ϵ_2=0.12, ϵ_4=0.005,1. Surface pressure, 2. Crossflow Mach number, 3. Crossflow Velocity.

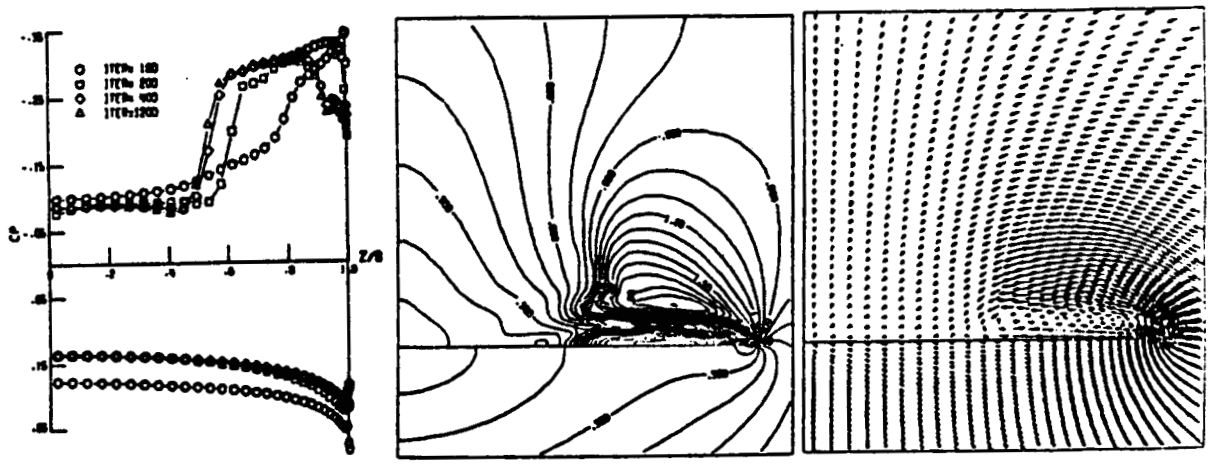

1 2 3

Figure 5. Standard Euler Set, numerical b.c., Round-edged Wing, 64X64 Cell, M_∞=2.0, α=10^0, β=70^0, ϵ_2=0.25, ϵ_4=0.01, 1. Surface pressure, 2. Crossflow Mach number, 3. Crossflow Velocity.

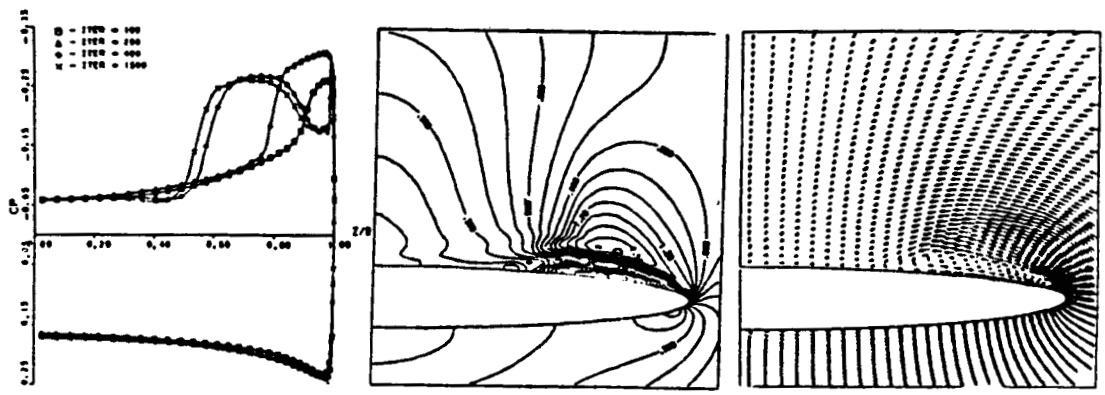

1 2 3

Figure 6. Zero-Total-Pressure-Loss Euler, Set (1), numerical b.c., round-edged Wing, 64X64 Cell, M_∞=2.0, α=10^0, β=70^0, ε_2=0.25, ε_4=0.01,1. Surface Pressure, 2. Crossflow Mach number, 3. Crossflow Velocity.

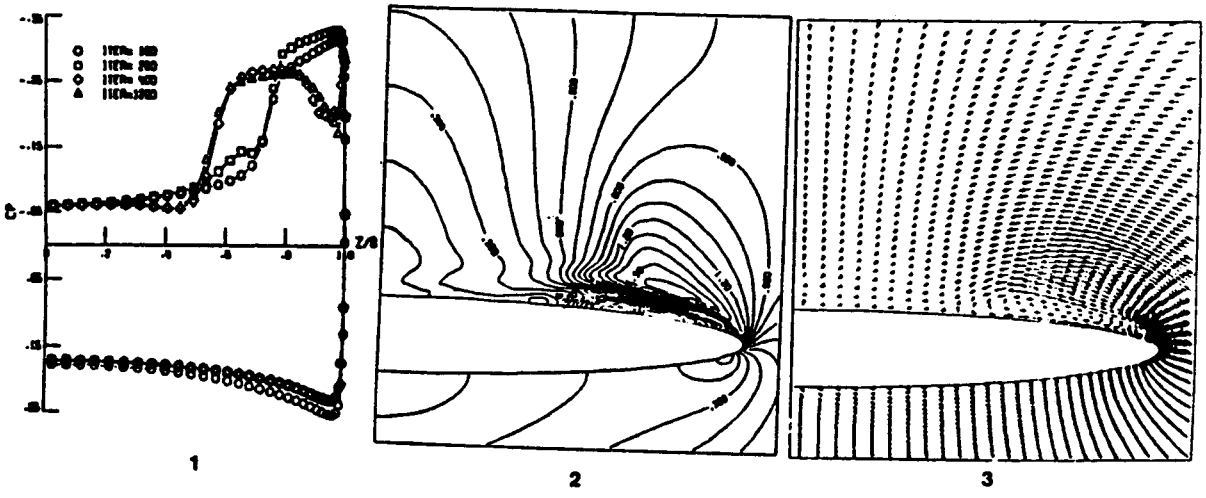

Figure 7. Standard Euler Set, C.f. b.c., round-edged wing, 64X64 cell, M_∞=2.0, α=10^0, β=70^0, ε_2=0.25, ε_4=0.01, 1. Surface pressure, 2. Crossflow Mach number, 3. Crossflow velocity.

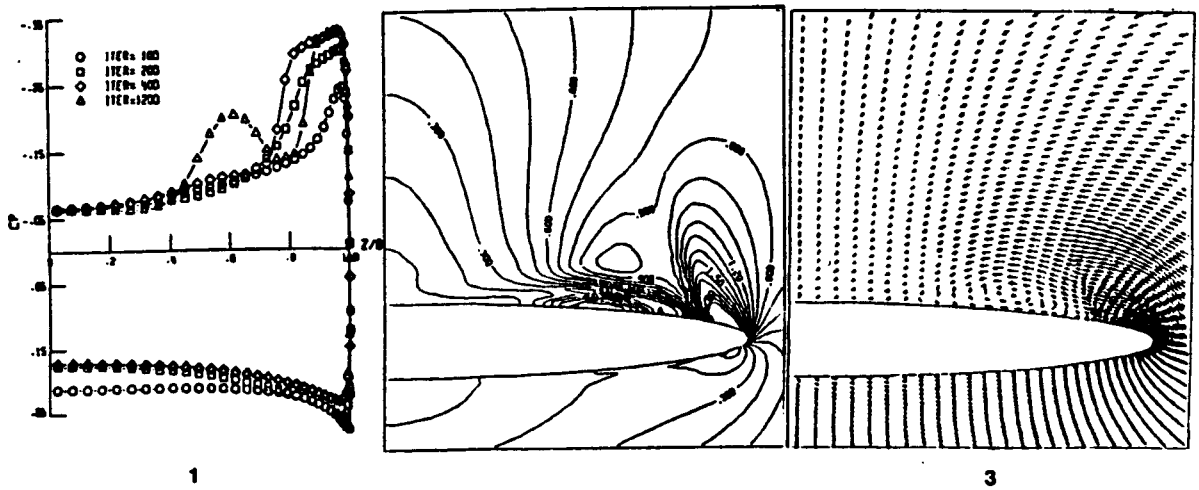

Figure 8. Zero-Total-Pressure-Loss Euler, Set (1), C.f. b.c., round-edged wing, 64X64 cell, M_∞=2.0, α=10°, β=70°, ϵ_2=0.25, ϵ_4=0.01, 1. Surface pressure, 2. Crossflow Mach number, 3. Crossflow Velocity.

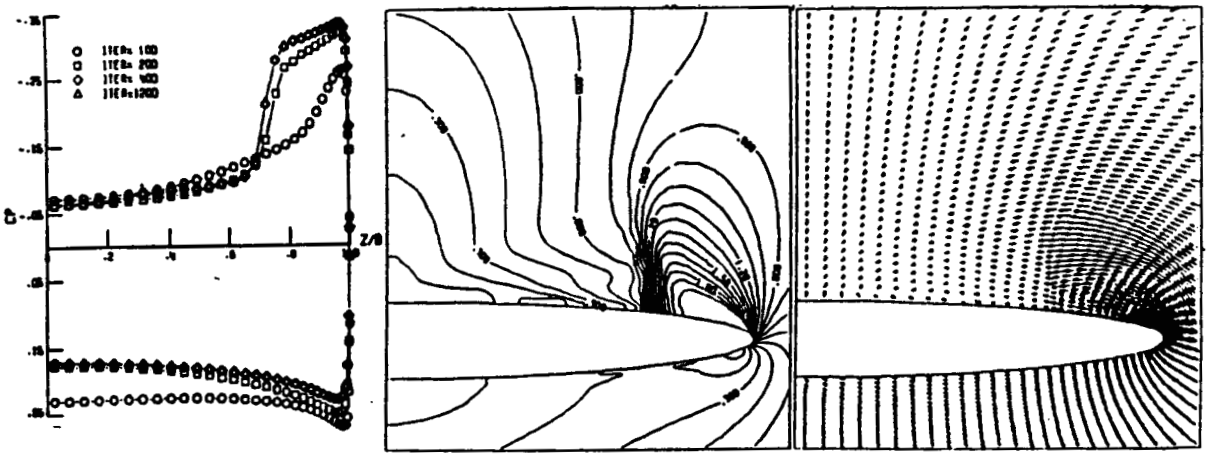

Figure 9. Standard Euler Set, numerical b.c., round-edged wing, 96X128 cell, M_∞=2.0, α=10°, β=70°, ϵ_2=0.25, ϵ_4=0.01,1. Surface pressure, 2. Crossflow Mach number, 3. Crossflow velocity.

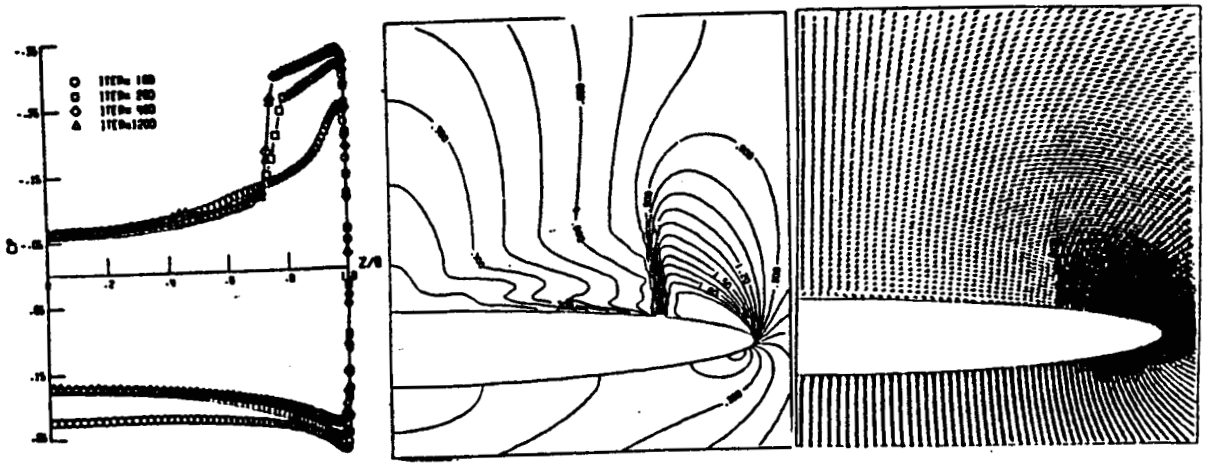

Figure 10. Zero-Total-Pressure-Loss Euler, Set (1), numerical b.c., round-edged wing, 96X128 cell, M_∞=2.0, α=10^0, β=70^0, ε_2=0.25, ε_4=0.01, 1. Surface pressure, 2. Crossflow Mach number, 3. Crossflow velocity.

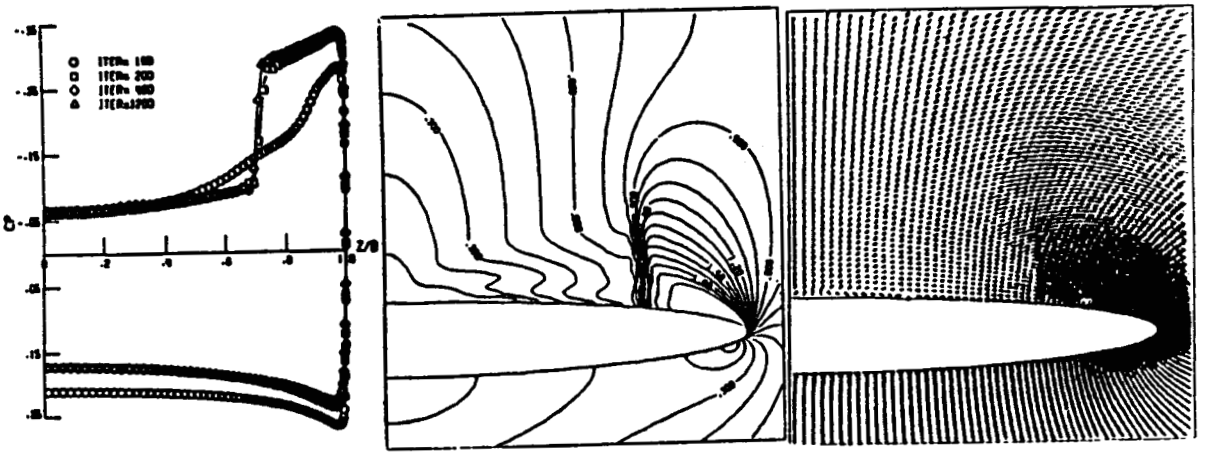

Figure 11. Standard Euler Set, C.F. b.c., round-edged wing, 96X128 cell, M_∞=2.0, α=10^0, β=70^0. ε_2=0.25, ε_4=0.01, 1. Surface pressure, 2. Cross flow Mach number, 3. Crossflow velocity.

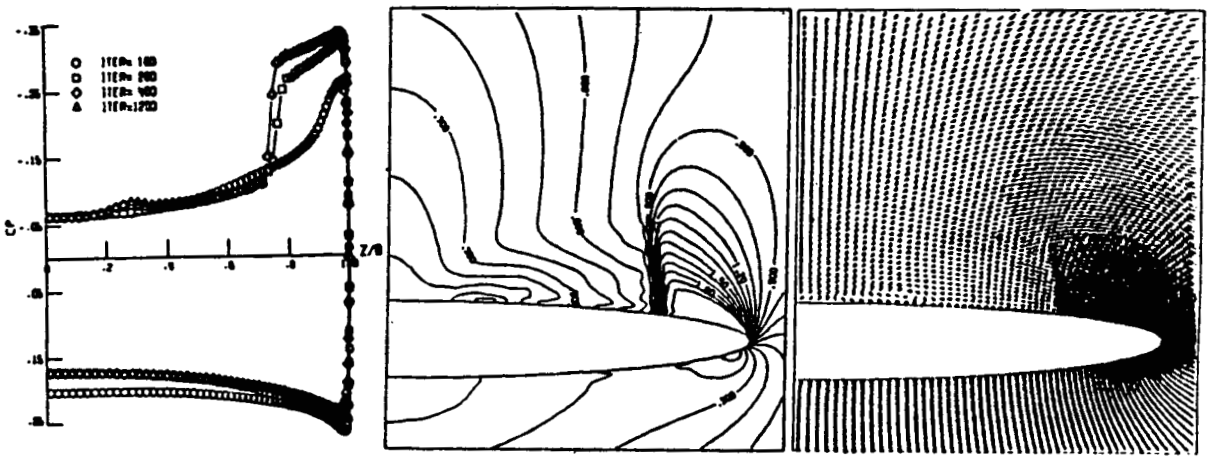

Figure 12. Zero-Total-Pressure-Loss Euler, Set (1), C. f. b.c., round-edged wing, 96X128 cell, M_∞=2.0, α=10^0, β=70^0, ϵ_2=0.25, ϵ_4=0.01, 1.Surface pressure, 2. Crossflow Mach number, 3. Crossflow velocity.

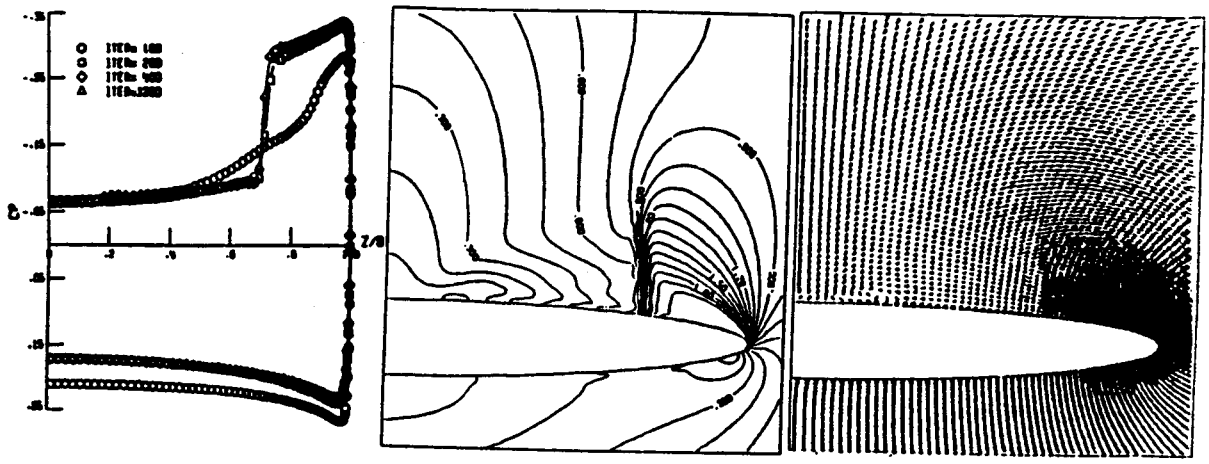

Figure 14. Three-Dimensional Transonic Flow, Standard Euler Set, Sharp-edged delta wing, 80X38X48 cell, M_∞=0.7, α=15^0, AR=1.5, ϵ_2=0.12, ϵ_4=0.005, (a.,b.) 1. Surface Pressure, 2. Static Pressure Contours, 3. Crossflow velocity (c.,d.)1.Static pressure Contours, 2. Crossflow velocity

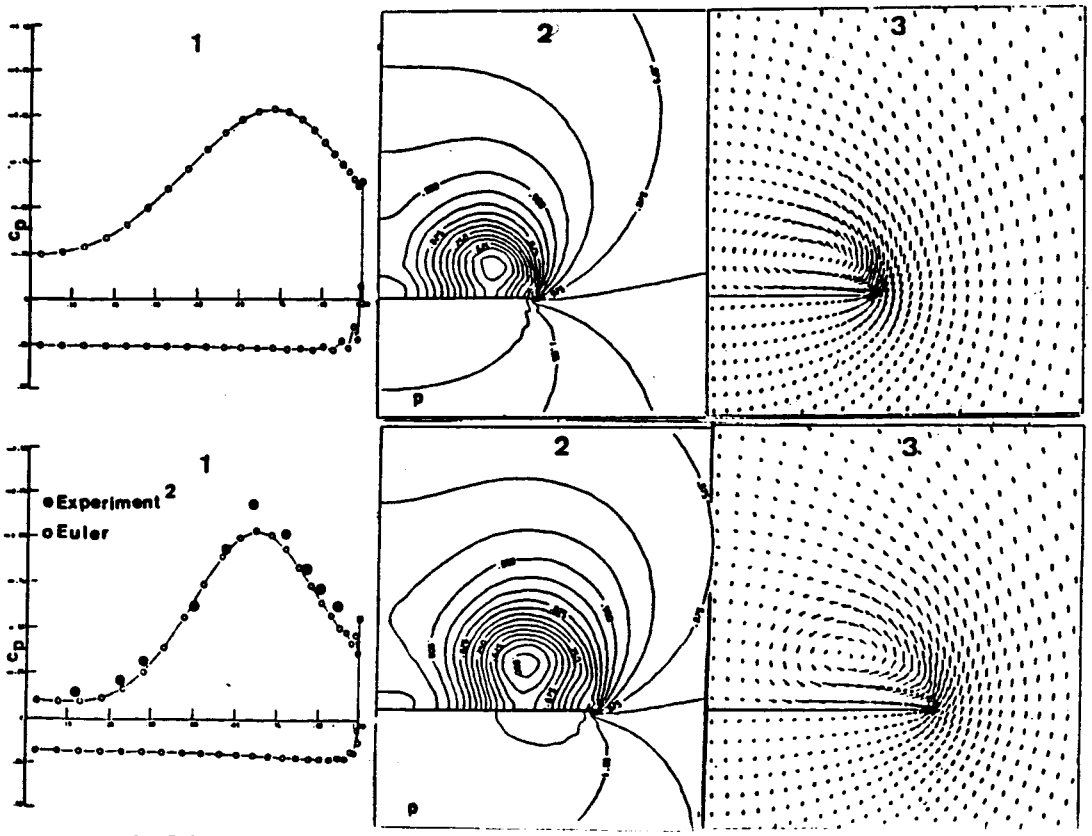

Figure 14. Three-Dimensional Transonic Flow, Standard Euler Set, Sharp-edged delta wing, 80X38X48 cell, M_∞=0.7, α=15^0, AR=1.5, ϵ_2=0.12, ϵ_4=0.005,
(a.,b.) 1. Surface Pressure, 2. Static Pressure Contours, 3. Crossflow velocity
(c.,d.)1. Static pressure Contours, 2. Crossflow velocity

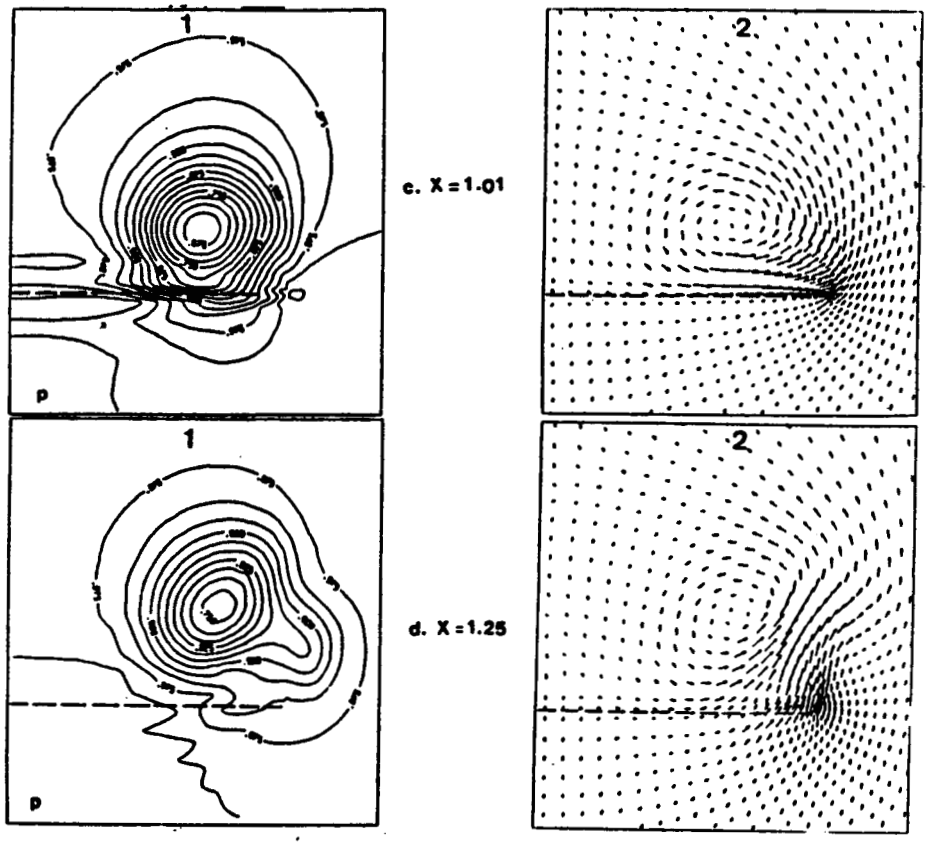

Figure 15. Three-Dimensional Transonic Flow, Standard Euler Set, Sharp-edged delta wing, 80X38X48 cell, M_∞=0.7, α=15^0, AR=1.5, ϵ_2=0.12, ϵ_4=0.005,

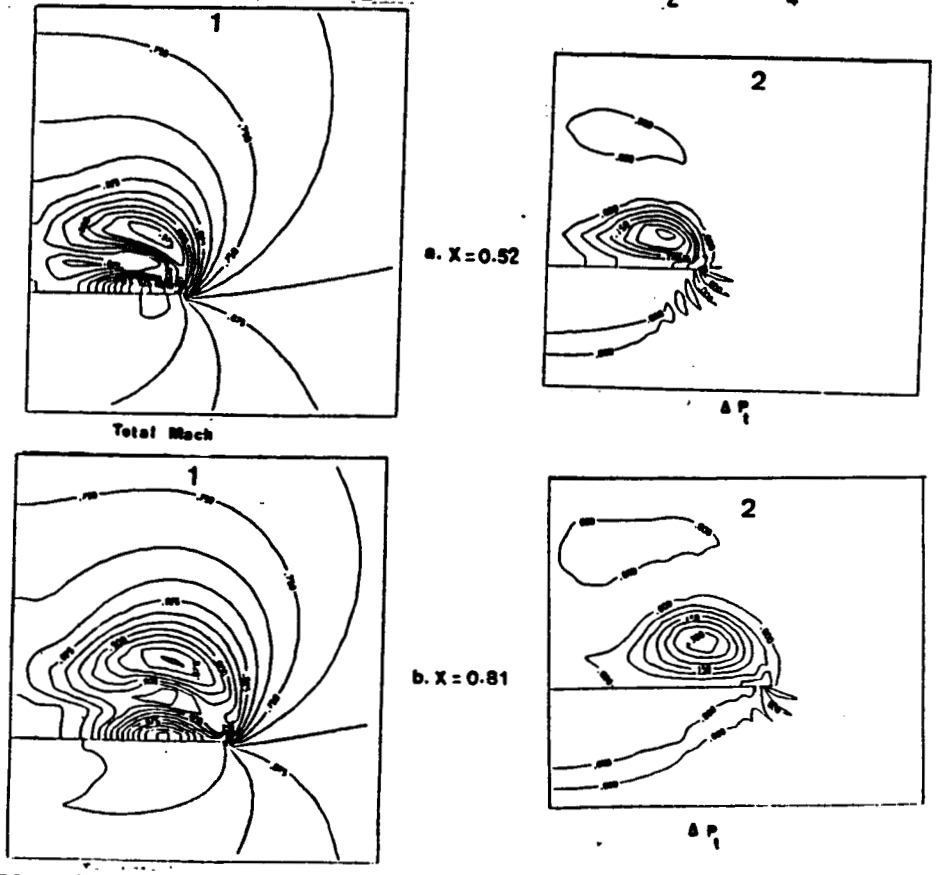

Figure 16. Three-dimensional subsonic flow, isentropic Euler set, sharp-edged delta wing, 80x38x48 cell, $M_\infty = 0.3$, $\alpha = 20.5°$, AR = 1, $\varepsilon_2 = 0.12$, $\varepsilon_4 = 0.005$, (a.,b.) 1. surface pressure, 2. static presure contours, C_p, 3. crossflow velocity

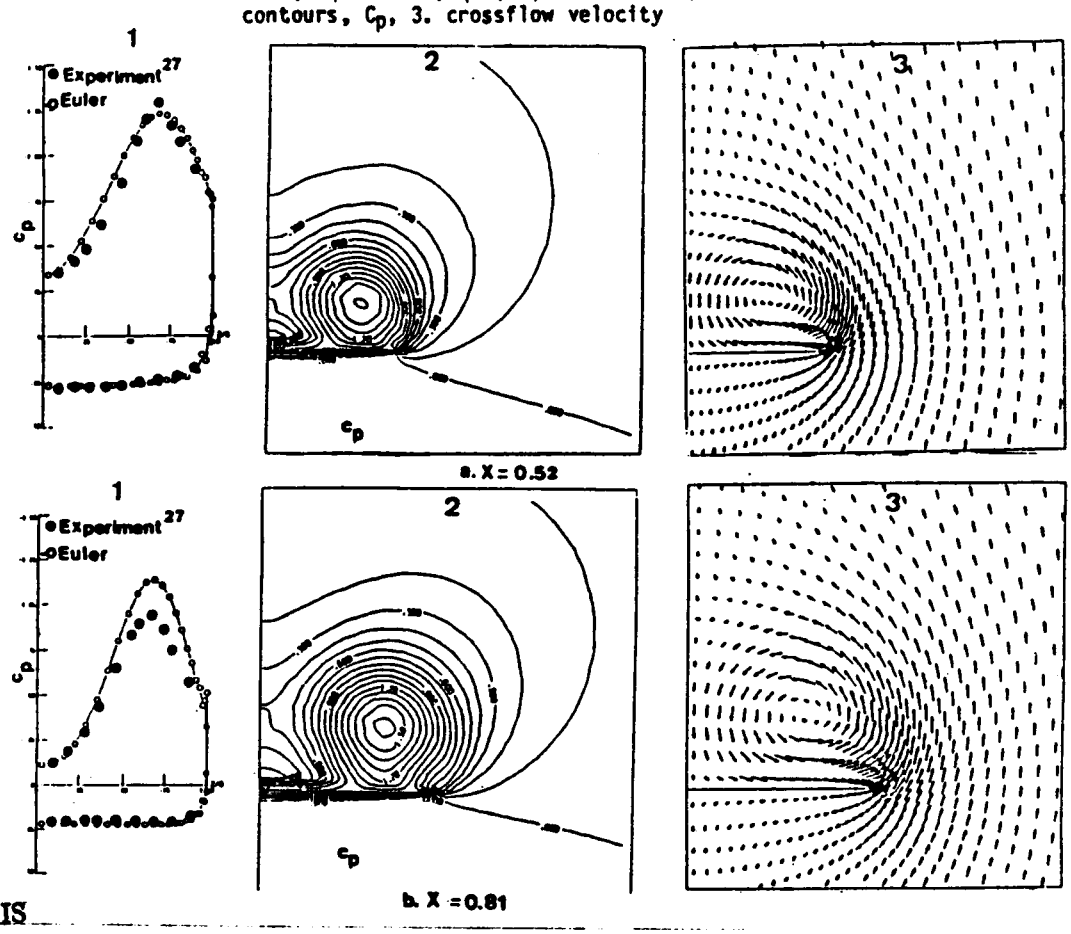

Figure 16. Three-dimensional subsonic flow, isentropic Euler set, sharp-edged delta wing, 80x38x48 cell, $M_\infty = 0.3$, $\alpha = 20.5°$, AR = 1, $\varepsilon_2 = 0.12$, $\varepsilon_4 = 0.005$, (c.d.) 1. experimental static pressure contours, C_p, (normal to wind direction), 2. static pressure contours, C_p, (normal to wing surface), 3. crossflow velocity.

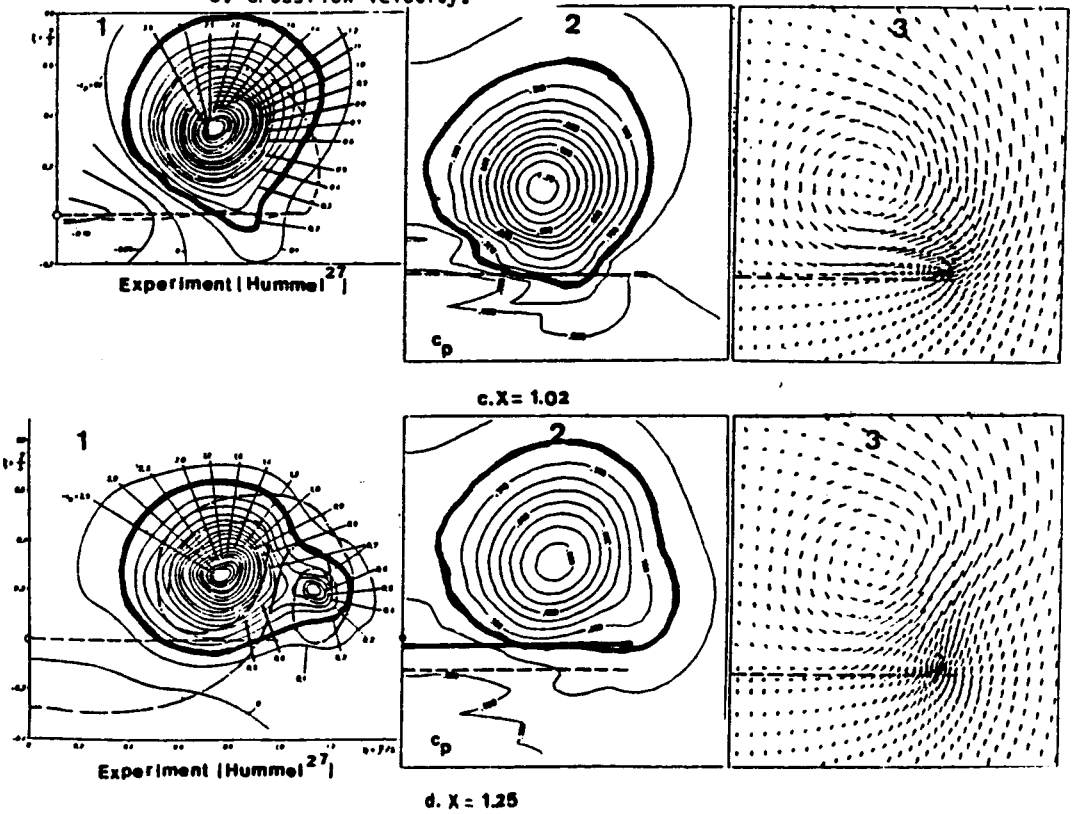

Numerical Examples (2)

flat- plate sharp-edged delta wing

- **Symmetric Conical Flow** (Classical Euler Eqs.)

  $M_\infty = 2$, $\alpha = 10^0$ and $\beta = 70^0$

- **Uniformly Rolling Wing a Conical Flow** (Classical Euler Eqs.)

$$\omega = \frac{\ell\omega^*}{U_\infty} = 0.5, \quad M_\infty = 2, \quad \alpha = 0^0 \text{ and } \beta = 70^0$$

- **Rolling Oscillation of a Wing in a Locally- Conical Flow** (Classical Euler Eqs.)

$$\bar{\omega} = -\omega_0 \cos kt\, \hat{e}_x, \text{ and } \theta = -\theta_{max} \sin kt$$

where

$$\theta_{max} = \omega_0/k \;, \quad K = \frac{k^*\ell}{U_\infty},$$

$$\omega_0 = 0.35, \theta_{max} = \pi/12, k = 1.337, M_\infty = 2, \alpha = 10^0 \text{ and } \beta = 70^0$$

$$\tau = 4.699$$

Fig. 1 Steady symmetric flow around a delta wing, $M_\infty=2$, $\alpha=10^0$, $\beta=70^0$

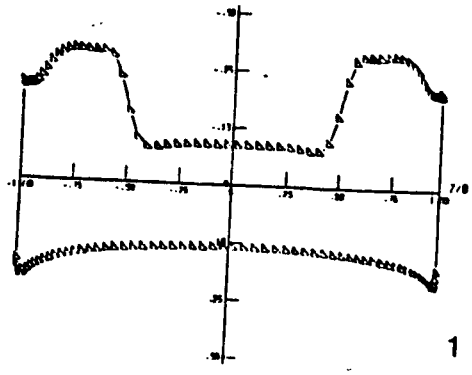

1. surface pressure

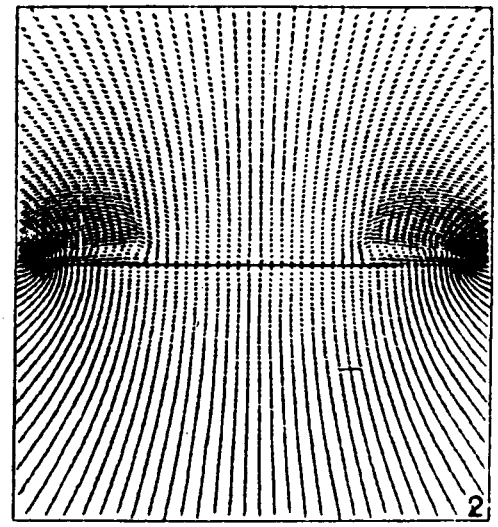

2. cross-flow velocity

Fig. 1 Steady symmetric flow around a delta wing, $M_\infty=2$, $\alpha=10^0$, $\beta=70^0$

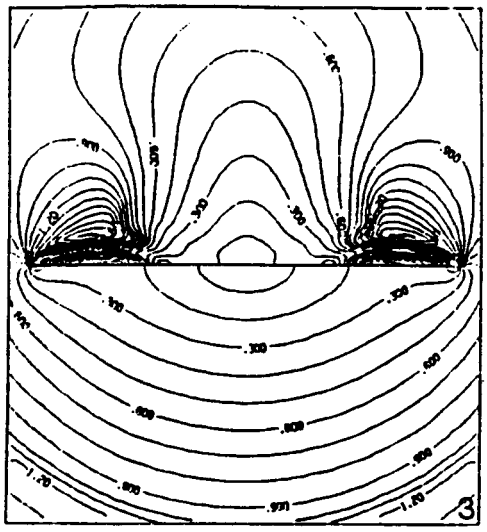

3. cross-flow Mach

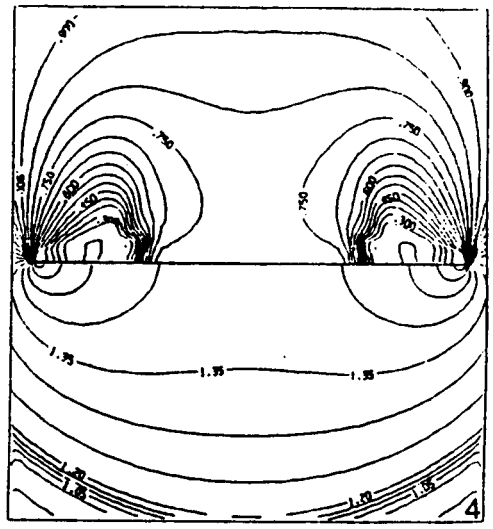

4. static pressure

Fig. 2. Uniform rolling of a delta wing, $M_\infty=2$, $\alpha=0^0$, $\beta=70^0$, $\omega=0.5$

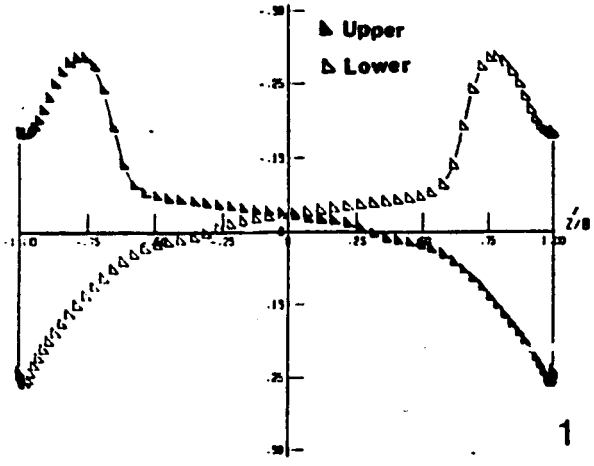

1. surface pressure

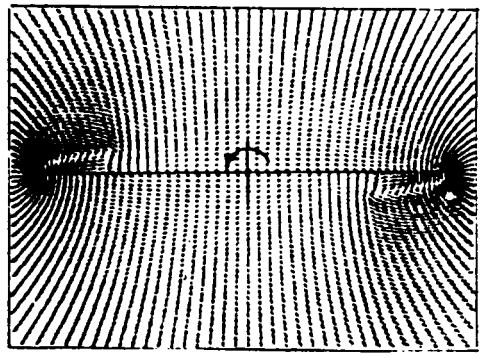

2. cross-flow velocity

Fig. 2. Uniform rolling of a delta wing.
$M_\infty=2$, $\alpha=0^0$, $\beta=70^0$, $\omega=0.5$

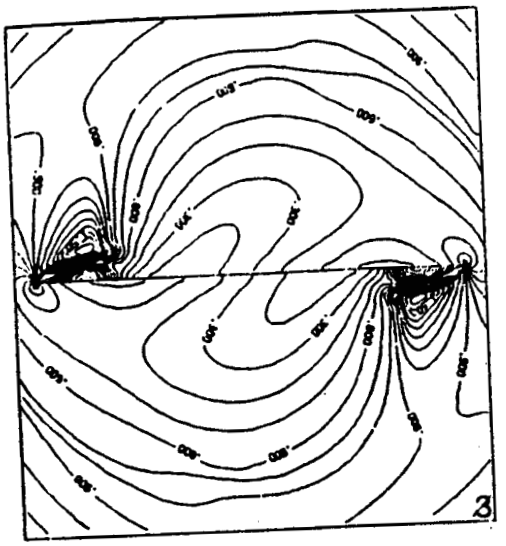

3. cross-flow Mach

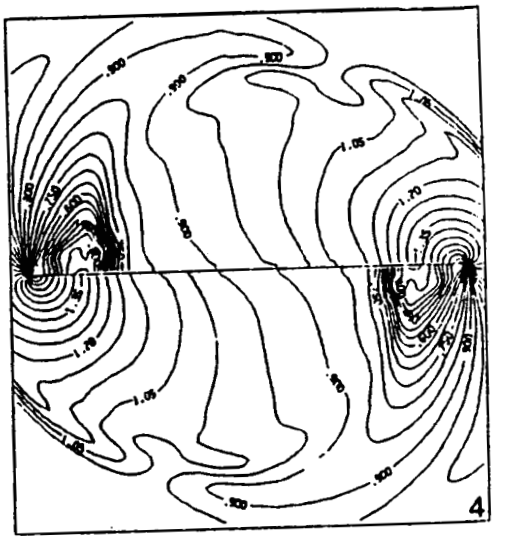

4. static pressure

Fig. 3 Roll angle, angular speed and angular acceleration of the rolling oscillation motion.

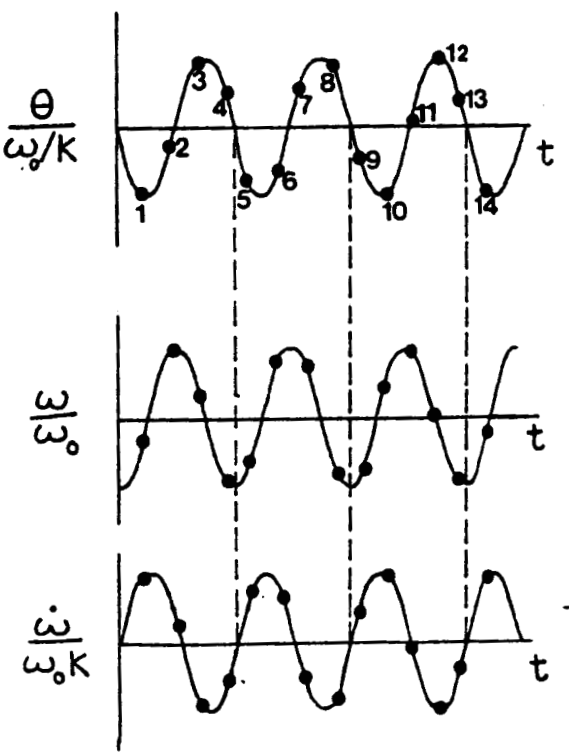

Point No.	Time	θ^0	Sense	Figure
1	1.07	-14.85	CCW	4
2	2.16	-3.76	CW	5
3	3.19	13.5	CW	6
4	4.31	7.46	CCW	7
5	5.35	-11.46	CCW	8
6	6.46	-10.63	CW	9
7	7.48	8.17	CW	10
8	8.59	13	CCW	11.1
9	9.69	-5.69	CCW	11.2
10	10.7	-14.79	CW	11.3
11	11.8	1.03	CW	11.4
12	12.8	14.8	CW	11.5
13	13.9	3.93	CCW	11.6
14	15.0	-14.01	CCW	11.7

Fig.4 . Rolling oscillation of a delta wing,
M_∞=2, α=10^0, β=70^0, ω=0.35, k=1.337,
θ_{max}=15^0, t=0-1.07, θ=0-(-14.85^0)

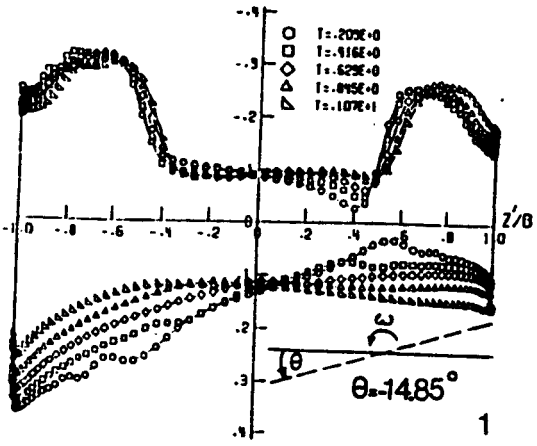

1. surface pressure

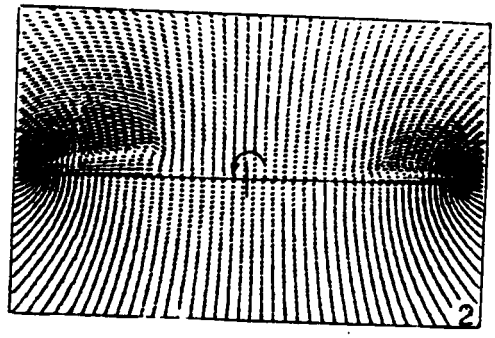

2. cross-flow velocity

Fig.4 . Rolling oscillation of a delta wing,
M_∞=2, α=10^0, β=70^0, ω=0.35, k=1.337,
θ_{max}=15^0, t=0-1.07, θ=0-(-14.85^0)

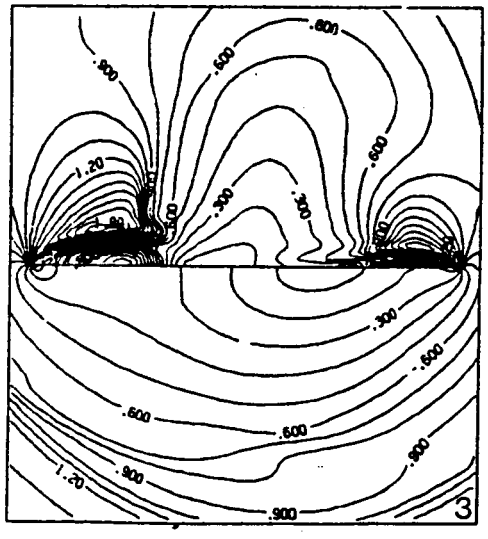

3. cross-flow Mach

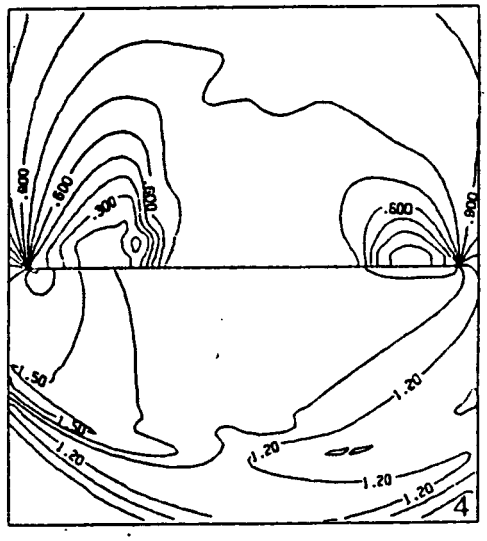

4. static pressure

...ig. 5. Rolling oscillation of a delta wing,
M_∞=2, α=10^0, β=70^0, ω=0.35, k=1.337,
θ_{max}=15^0, t=1.07$^+$-2.16, θ=(-14.85^0)-(-3.76°)

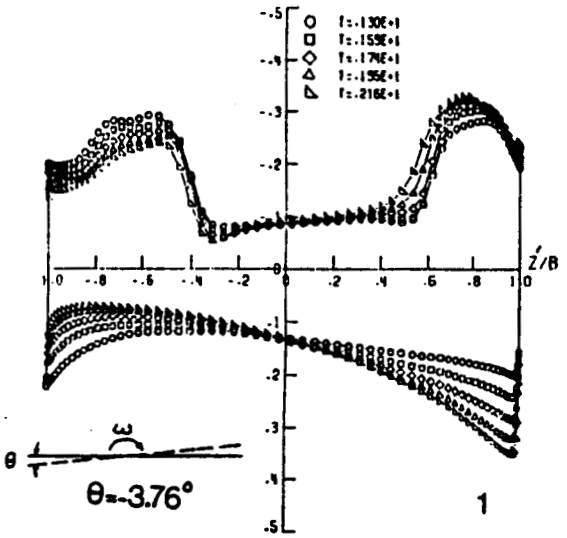

1. surface pressure

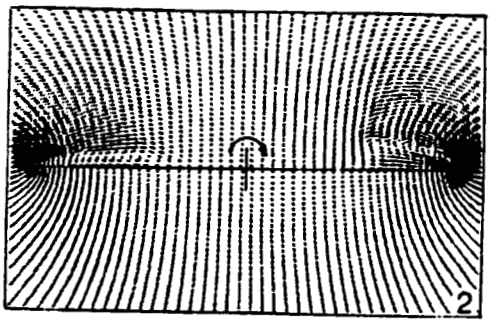

2. cross-flow velocity

ORIGINAL PAGE IS
OF POOR QUALITY

Fig. 5. Rolling oscillation of a delta wing,
M_∞=2, α=10^0, β=70^0, ω=0.35, k=1.337,
θ_{max}=15^0, t=1.07$^+$-2.16, θ=(-14.85^0)-
(-3.76°)

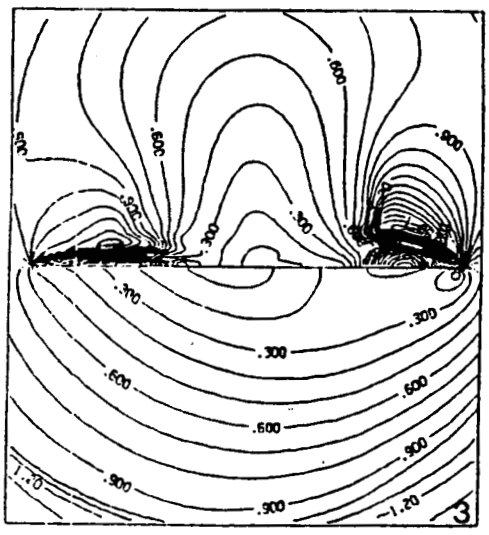

3. cross-flow Mach

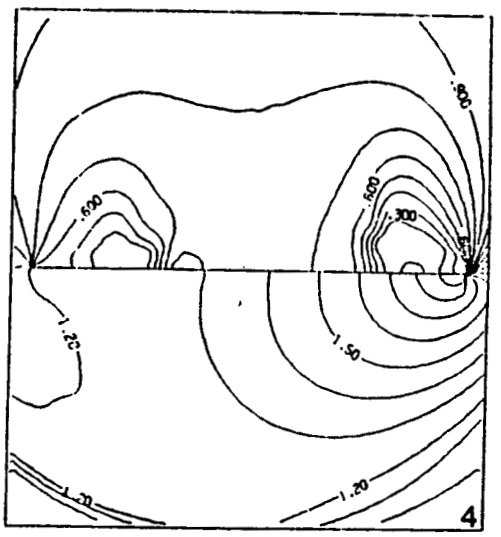

4. static pressure

Fig. 6. Rolling oscillation of a delta wing, $M_\infty=2$, $\alpha=10^0$, $\beta=70^0$, $\omega=0.35$, $k=1.337$, $\theta_{max}=15^0$, $t=2.16^+-3.19$, $\theta=(-3.76^0)-(+13.5^0)$

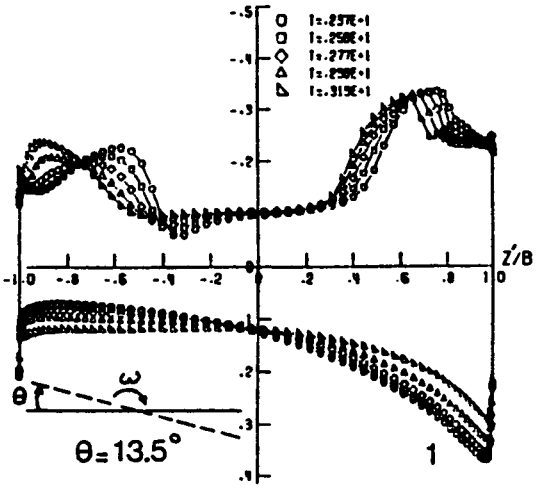

1. surface pressure

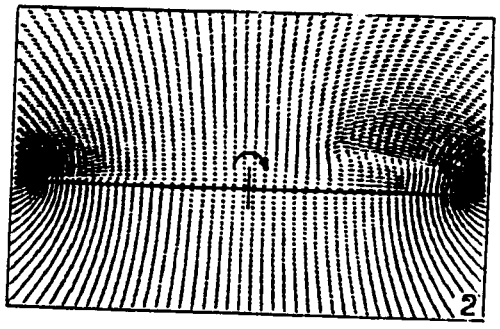

2. cross-flow velocity

Fig. 6. Rolling oscillation of a delta wing, $M_\infty=2$, $\alpha=10^0$, $\beta=70^0$, $\omega=0.35$, $k=1.337$, $\theta_{max}=15^0$, $t=2.16^+-3.19$, $\theta=(-3.76^0)-(+13.5^0)$

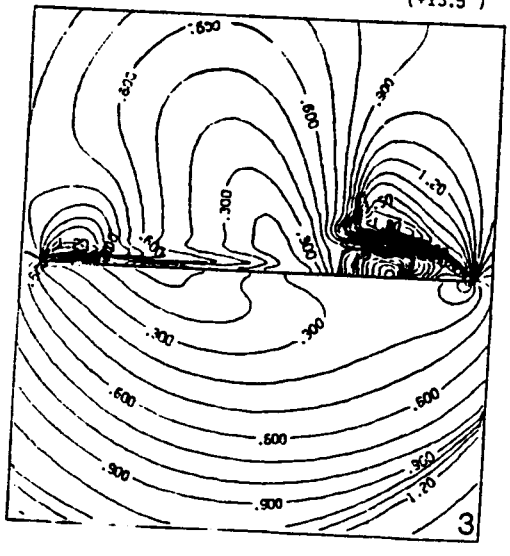

3. cross-flow Mach

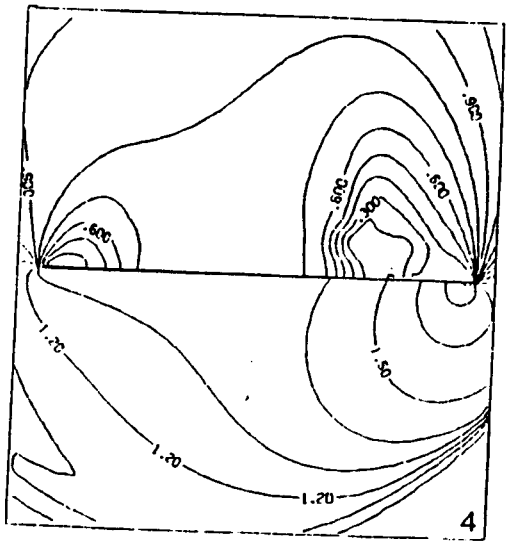

4. static pressure

Fig. 7. Rolling oscillation of a delta wing,
$M_\infty=2$, $\alpha=10^0$, $\beta=70^0$, $\omega=0.35$, $k=1.337$,
$\theta_{max}=15^0$, $t=3.19^+-4.31$, $\theta=(+13.5^0)-(+7.46^0)$

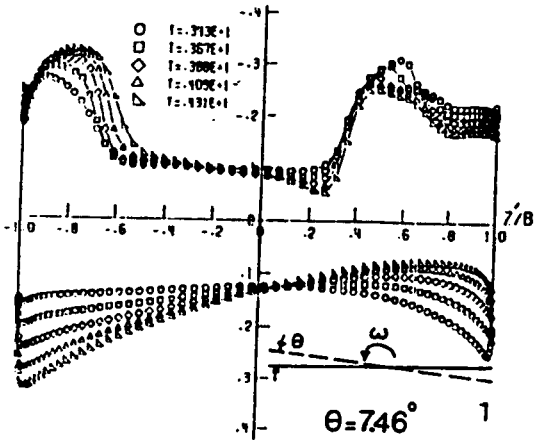

1. surface pressure

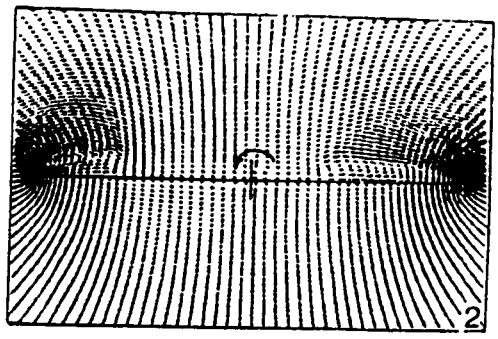

2. cross-flow velocity

Fig. 7. Rolling oscillation of a delta wing,
$M_\infty=2$, $\alpha=10^0$, $\beta=70^0$, $\omega=0.35$, $k=1.337$,
$\theta_{max}=15^0$, $t=3.19^+-4.31$, $\theta=(+13.5^0)-(+7.46^0)$

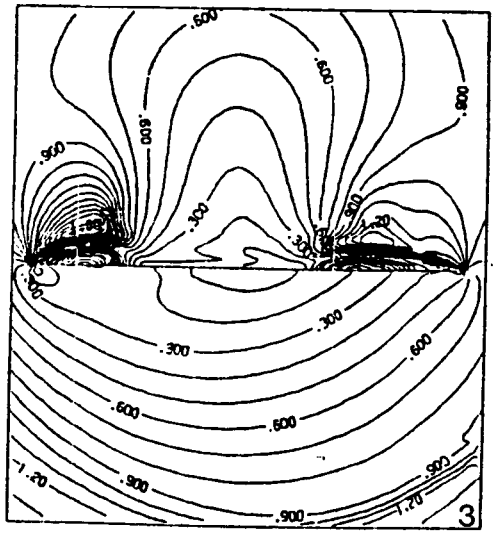

3. cross-flow Mach

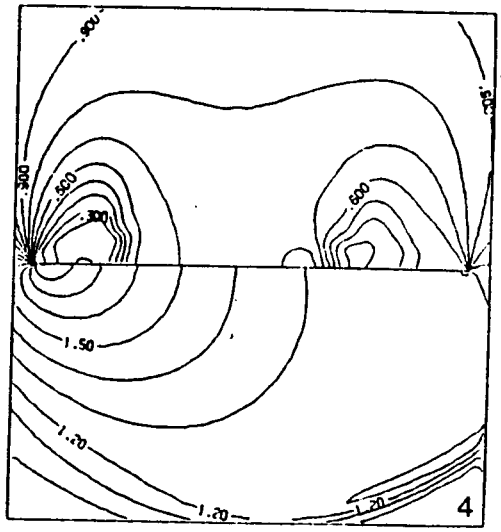

4. static pressure

Fig. 8. Rolling oscillation of a delta wing, $M_\infty=2$, $\alpha=10^0$, $\beta=70^0$, $\omega=0.35$, $k=1.337$, $\theta_{max}=15^0$, $t=4.31^+-5.35$, $\theta=(+7.46^0)-(-11.46^\circ)$

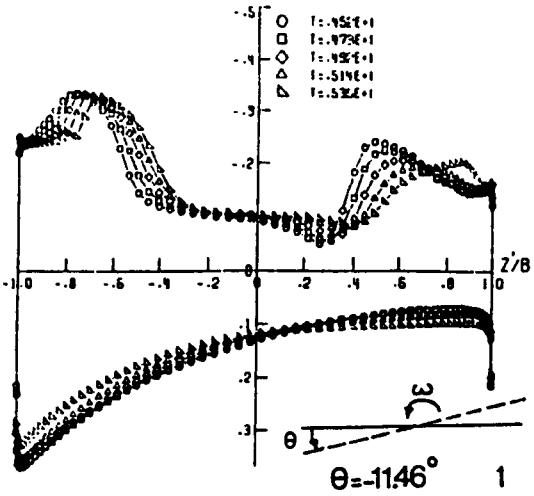

1. surface pressure

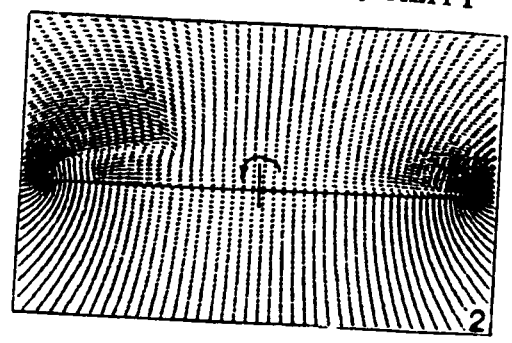

2. cross-flow velocity

Fig. 8. Rolling oscillation of a delta wing, $M_\infty=2$, $\alpha=10^0$, $\beta=70^0$, $\omega=0.35$, $k=1.337$, $\theta_{max}=15^0$, $t=4.31^+-5.35$, $\theta=(+7.46^0)-(-11.46^\circ)$

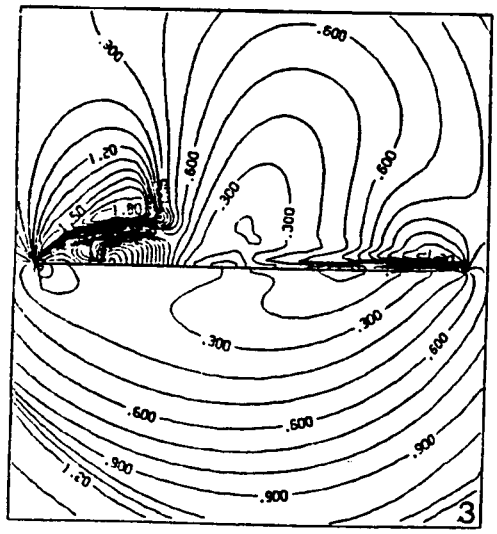

3 cross-flow Mach

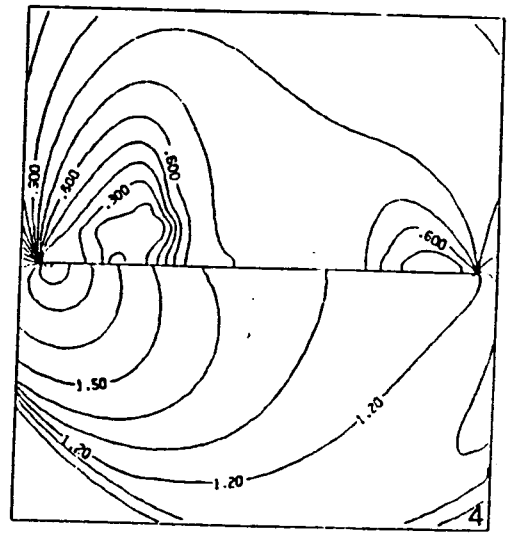

4. static pressure

Fig. 9. Rolling oscillation of a delta wing, $M_\infty=2$, $\alpha=10^0$, $\beta=70^0$, $\omega=0.35$, $k=1.337$, $\theta_{max}=15^0$, $t=5.35^+-6.46$, $\theta=(-11.46^0)-(-10.63^0)$

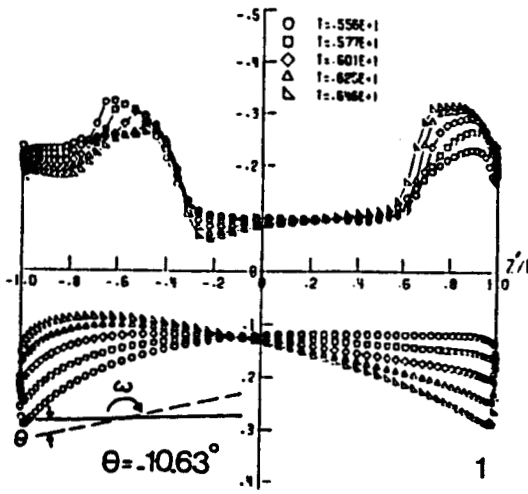

1. surface pressure

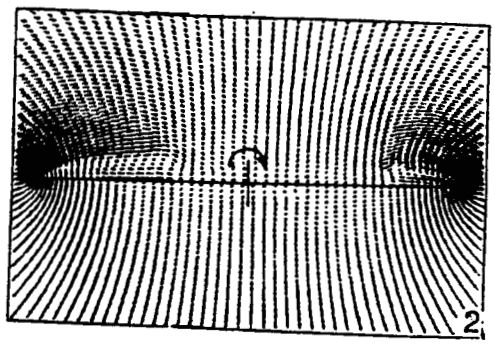

2. cross-flow velocity

Fig. 9. Rolling oscillation of a delta wing, $M_\infty=2$, $\alpha=10^0$, $\beta=70^0$, $\omega=0.35$, $k=1.337$, $\theta_{max}=15^0$, $t=5.35^+-6.46$, $\theta=(-11.46^0)-(-10.63^0)$

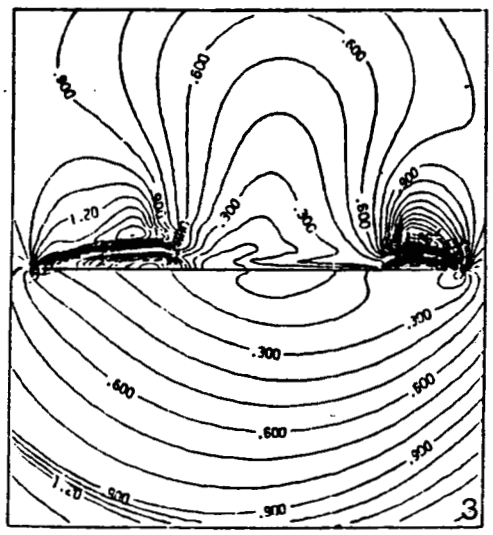

3. cross-flow Mach

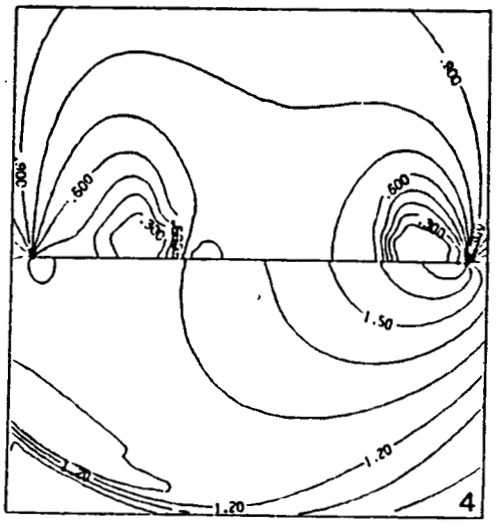

4. static pressure

Fig. 10. Rolling oscillation of a delta wing,
$M_\infty=2$, $\alpha=10^0$, $\beta=70^0$, $\omega=0.35$, $k=1.337$,
$\theta_{max}=15^0$, $t=6.46^+-7.48$, $\theta=(10.63^0)-(+8.17^\circ)$

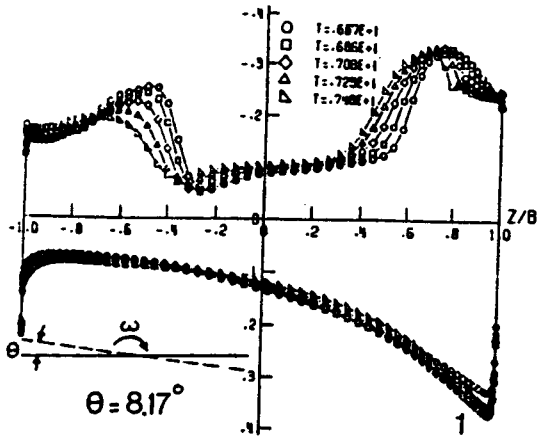

1. surface pressure

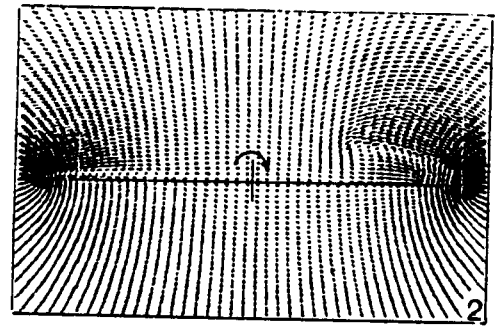

2. cross-flow velocity

Fig. 10. Rolling oscillation of a delta wing,
$M_\infty=2$, $\alpha=10^0$, $\beta=70^0$, $\omega=0.35$, $k=1.337$,
$\theta_{max}=15^0$, $t=6.46^+-7.48$, $\theta=(10.63^0)-(+8.17^\circ)$

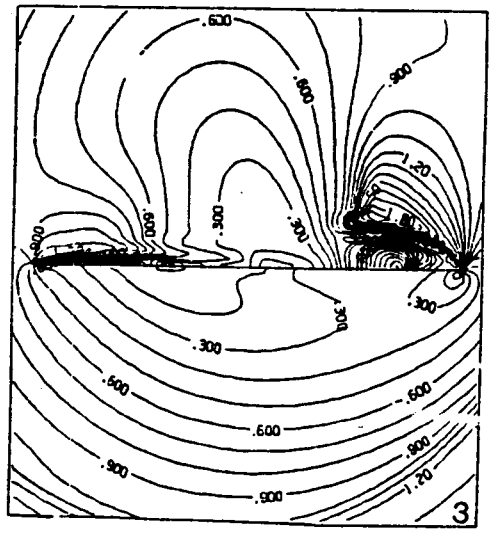

3. cross-flow Mach

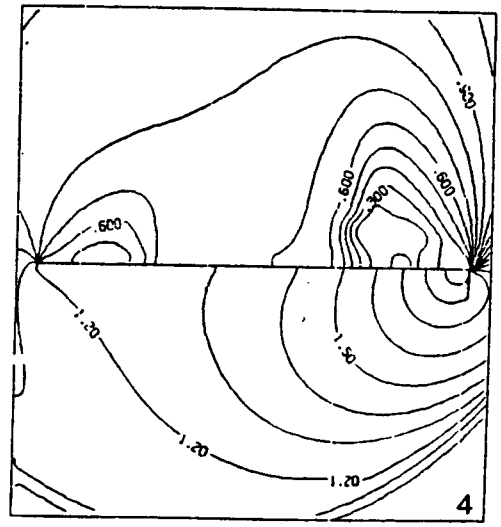

4. static pressure

Fig. 11 Rolling oscillations from t = 7.48+ to t = 15.0, steady state oscillation is reached.

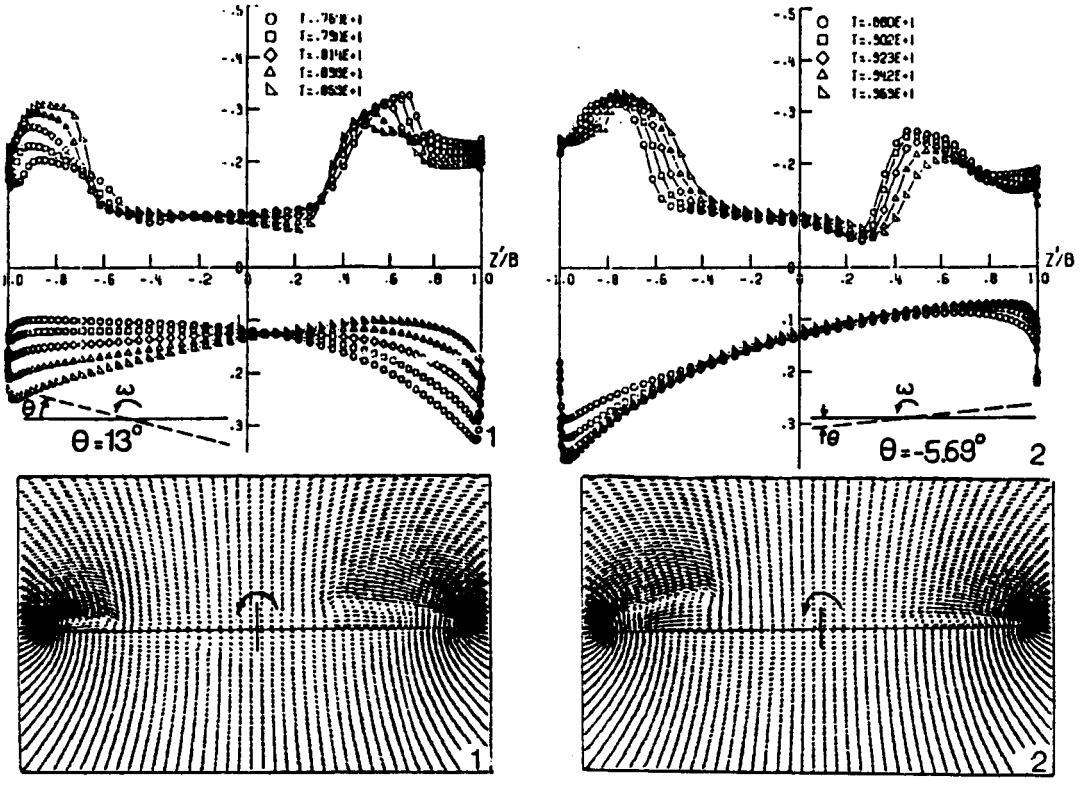

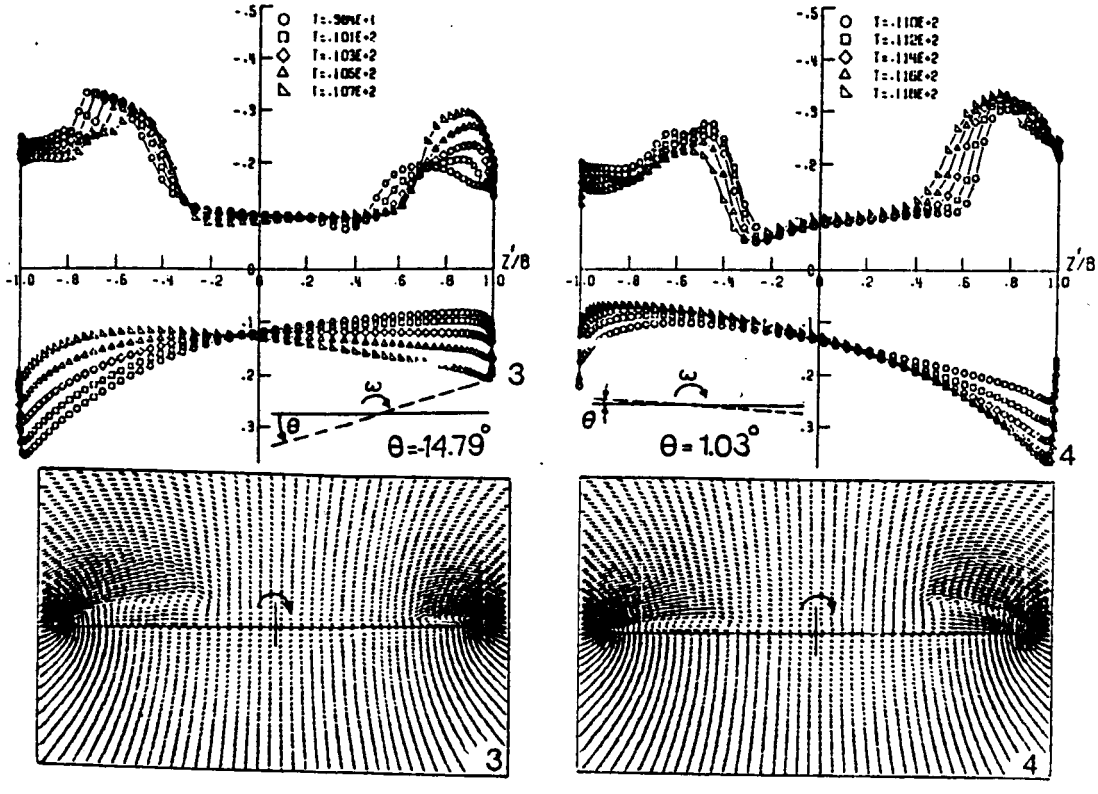

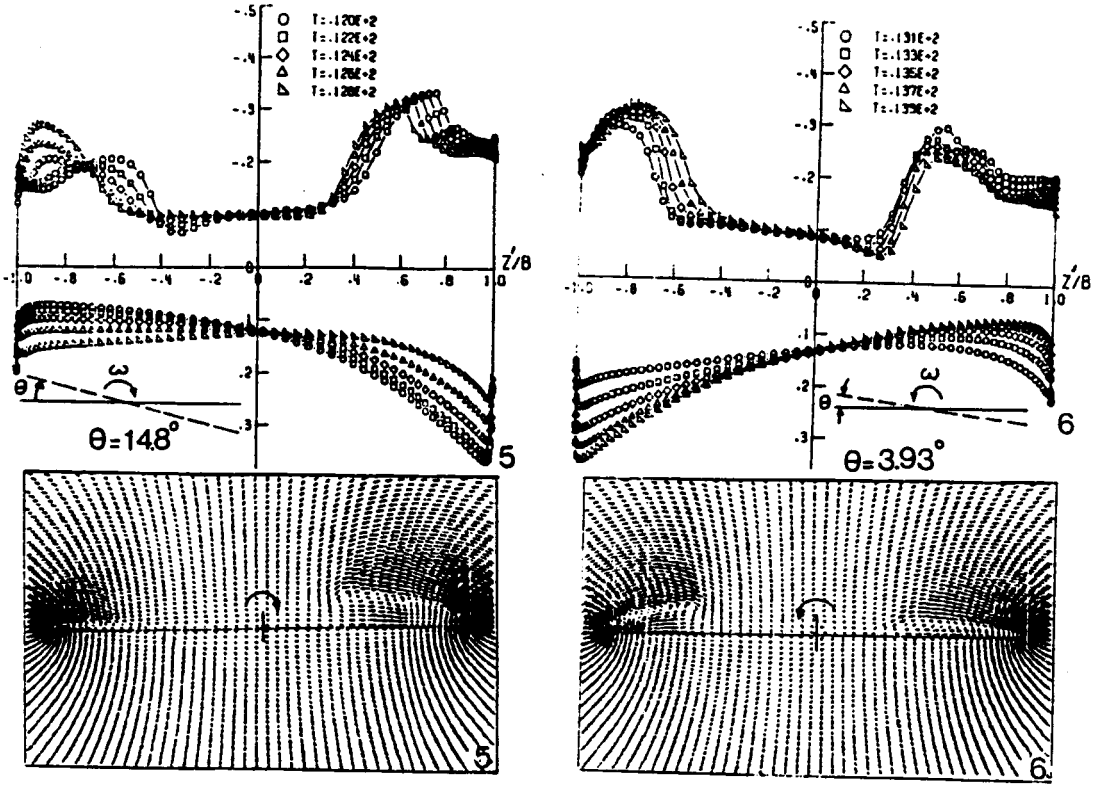

Fig. 11 Rolling oscillations from t = 7.48* to t = 15.0, steady state oscillation is reached.

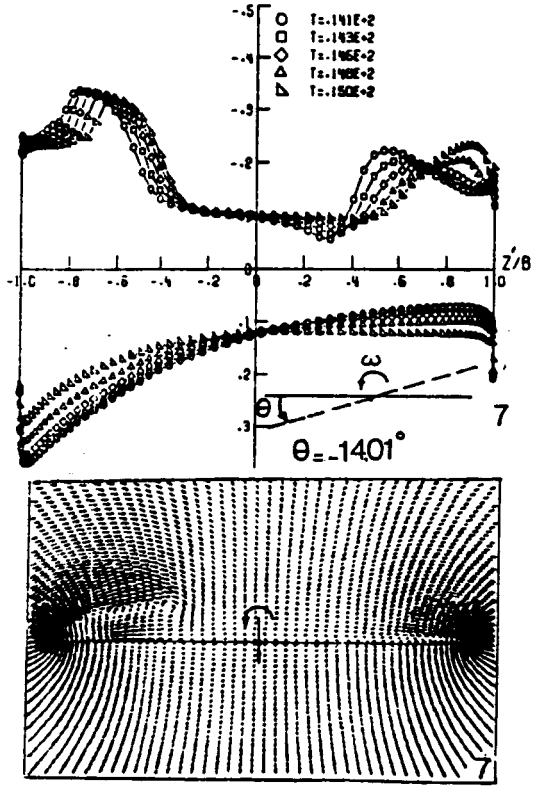

FIGURE 14. TIME HISTORY OF THE LIFT AND ROLLING-MOMENT COEFFICIENTS

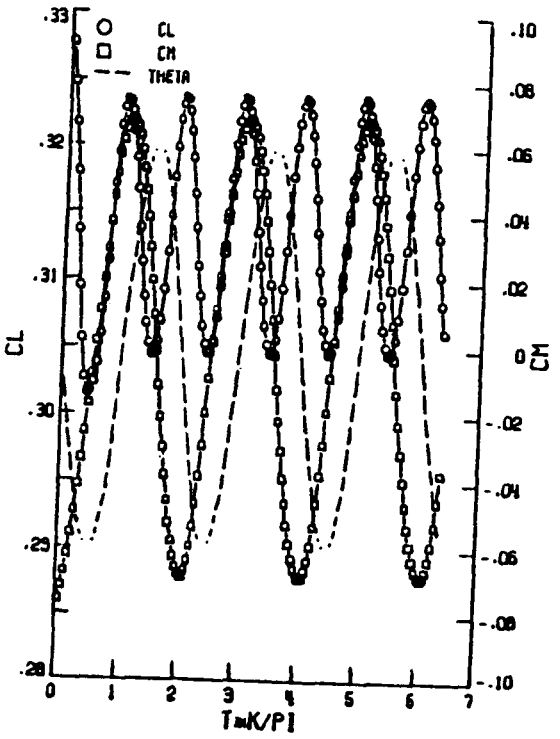

CONCLUDING REMARKS

1. WE HAVE PRESENTED APPLICATIONS OF THE CLASSICAL AND ZERO-TOTAL-PRESSURE-LOSS SETS OF EULER EQUATIONS TO SHARP- AND ROUND-EDGED DELTA WINGS.

2. WE HAVE EXPLAINED THE ORIGIN OF THE TOTAL PRESSURE LOSS IN THE CLASSICAL SET .

3. FOR SHARP-EDGED DELTA WINGS, ALL SETS OF EULER EQUATIONS PRODUCE THE SAME SEPARATED FLOW SOLUTIONS. THE SOLUTIONS REPRESENT REAL FLOW SOLUTIONS.

4. FOR ROUND-EDGED DELTA WINGS AND FOR COARSE GRIDS, THE SOLUTION DEPENDS ON (1) THE LEVEL OF DISSIPATION, (2) THE ACCURACY OF THE SURFACE BOUNDARY CONDITION, AND (3) THE TYPE OF EULER EQS. SET. ONE CAN GET SEPARATED, PARTIALLY SEPARATED, OR ATTACHED FLOW SOLUTIONS.

5. FOR ROUND-EDGED DELTA WINGS AND FOR FINE GRIDS, ATTACHED FLOW SOLUTIONS ARE OBTAINED.

6. WE HAVE ALSO PRESENTED THREE-DIMENSIONAL FLOW SOLUTIONS AND ASYMMETRIC FLOW SOLUTIONS INCLUDING UNSTEADY FLOWS FOR SHARP-EDGED DELTA WINGS.

7. EULER EQS. SHOULD BE RESTRICTED TO SHARP-EDGED WINGS FOR REAL FLOW SOLUTIONS. FOR ROUND-EDGED WINGS, NAVIER-STOKES EQS. MUST BE USED.